SUPPLEMENTAL INFORMATION

Sub-micrometre two- and three-dimensional insights into Earth's oldest stromatolites (ca. 3.5 Ga): prospects for the search for life on Mars

Keyron Hickman-Lewis, Barbara Cavalazzi, Konstantinos Giannoukos, Lorenzo d'Amico, Stevan Vrbaski, Giulia Saccomano, Diego Dreossi, Giuliana Tromba, Frédéric Foucher, Will Brownscombe, Caroline L. Smith, Frances Westall

Correspondence to KHL at keyron.hickman-lewis@nhm.ac.uk

METHODS

Fieldwork and sampling

Samples were collected during a field campaign in 2000 from the lowermost horizons of the chert–barite sequence (DFc1) Dresser Formation at North Pole Dome, East Pilbara, Western Australia. Stromatolites were observed in horizons corresponding to lithostratigraphic assemblages A1–A2 in Van Kranendonk et al. (2018), revised as LA1–LA2 in Djokic et al. (2021). Stromatolitic horizons are intercalated with chert–barite layers; larger chert–barite veins cross-cut the sequence (*cf.* Tadbiri and Van Kranendonk, 2020).

Sample preparation

Samples were prepared as petrographic thin sections for optical microscopy, Raman spectroscopy, SEM-EDX and laser ablation (LA) ICP-MS, and as 10 mm and 2 mm diameter cylinders for laboratory X-ray µCT and synchrotron µCT analyses, respectively. Cylindrical samples are crucial for minimizing edge artefacts in reconstructed high-resolution tomographic datasets.

Optical microscopy

Optical photomicrographs were acquired at the Imaging and Analyses Centre, Natural History Museum (London), using an Olympus BX63 optical microscope equipped with a CCD camera. Images were processed using CellSens software.

LA ICP-MS

Spatially resolved trace element concentrations were determined using Laser Ablation Inductively Coupled Mass Spectrometry (LA ICP-MS) on a 193 nm ESI Laser Ablation System coupled to an Agilent 7700 ICP-MS at the Natural History Museum, London. All analyses were conducted on microcrystalline quartz that was visibly free of other phases that may have modified or contaminated the compositional signal. NIST 612 was used as an external standard and NIST 610 and GSD-1G were used as secondary standards. Data were collected for 40 s using a spot size of 60 µm and laser fluence of 2.5 J/cm^2 at a frequency of 5 Hz.

All elements gave secondary standard values within 10% of reported values. REE+Y concentrations were normalized using Mud of Queensland (MUQ; Kamber et al., 2006) values. La, Eu, Gd and Y anomalies (X/X*, where X is the element of interest) were calculated

according to the methods of Lawrence et al. (2006) and Lawrence and Kamber (2006) as follows:

$La/La* = La/(Pr \times (Pr/Nd)^2)$ Eq. 1
$Y/Y* = Y/(0.5 \times Er + 0.5 \times Ho)$ Eq. 2
$Gd/Gd* = Gd/(((Tb^2) \times Sm)^{0.33})$ Eq. 3
$Eu/Eu* = Eu/(((Sm^2) \times Tb)^{0.33})$ Eq. 4

In all equations above, the subscript N denotes that MuQ-normalized values should be used in the calculations.

SEM-EDX

SEM BSE imaging and EDX phase mapping of a carbon-coated stromatolitic thin section was conducted at the Imaging and Analyses Centre Natural History Museum, London, using a TESCAN integrated Mineral Analyser SEM (TIMA) operating at 25 kV and 13.41 nA. The thin section was scanned at a resolution of 4 μm/pixel over 14 hours acquiring 55 million EDX spectra. One hundred and fifty fields of interest were rescanned at 2 μm pixel resolution lasting 10 hours and acquiring a further 37.5 million EDX spectra. Spectra were assigned to mineral classifications defined from this studied suite of samples.

Raman spectroscopy

Raman spectroscopy was conducted with a WITec Alpha500 RA system using a frequency-doubled Nd:YAG green laser (wavelength 532 nm) at CNRS-CBM (CNRS Orléans). The system uses a motorized table to move the sample continuously below a laser beam focussed onto the sample via a microscope objective (50x). Spectra form a dataset, spatially referenced over the scanned area, which was processed to obtain compositional maps in which compounds are represented as a range of colours.

Laboratory X-ray μCT

Acquisition:
Micro-CT examination was performed at Elettra Sincrotrone (Trieste, Italy) using a custom-made CT system equipped with a microfocus sealed Hamamatsu L12161-07 X-ray source operating at 90 kV and 85 μA with a 1 mm Al filter. The focal spot was set to 7 μm. The focus to sample distance was 80 mm and the focus to detector distance was 308 mm. The rotation step was 0.2 deg over 360 deg and 1801 projections were acquired. A Photonics CCD camera detector with an isotropic pixel size of 12.5 μm was used. With 2*2 binning, the effective pixel size was 6.5 μm.

Reconstruction:
Data reconstruction was performed using NRecon v1.7.0.4 by Bruker (2012–2016). The beam hardening correction was optimized to 23% and the ring artefact parameter was set to 13. The calibrated camera rotation (theta) was found to be 0.30 degrees.

Segmentation:
The reconstructed volume of the scanned dataset was processed using Dragonfly 2020.1.1 (software available at http://www.theobjects.com/dragonfly). Four phases, namely hematite, barite, quartz and pore spaces, were segmented. Firstly, the 3D unsharp filter was used with a

kernel size of 3 px and an unsharp factor of 5. Secondly, a median filter with a kernel size of 3 px was applied. The second filter was found to have no impact on the very fine structure of hematite. Investigation of the overall histogram did not show easily separable peaks to allow direct phase segmentation. The histogram shown in Figure S13 demonstrates this overlap between phases; this is evidence of a highly heterogeneous composition, likely arising from the heterogeneous diffusion of each phase into adjacent phases during the complex greenschist grade metamorphic history of the samples (Dunlop et al., 1978; Buick et al., 1981; Van Kranendonk, 2006). Localized analyses between the phases allowed the clear deconvolution of each phase and enabled the entirety of the sample to be successfully segmented. In general, grey values above 50,570 corresponded to hematite, grey values from 50,570 to 15,364 corresponded to barite, grey values from 15,364 to 1,100 corresponded to quartz, and grey values below 1,100 corresponded to pores. These values were measured from the intensity profiles across segments at the borders of the various phases according to full width at half maximum analysis (Amado et al., 2004) Phases segmentation is shown in Figures S14–S15. Either the gamma ratio or gamma correction was used to adjust the perception of the pixels of each phase (Kaufmann, 2012).

Synchrotron μCT

Synchrotron μCT was performed at the SYRMEP beamline of the Elettra synchrotron light source (Trieste, Italy). The beam originates from a bending magnet providing a beam in a nearby parallel geometry. The sample was positioned at a distance of 23 m from the source. CT scans were performed in propagation-based phase contrast mode with a sample-to-detector distance of 15 cm. The white beam was filtered using 1.5 mm of silica and 1 mm of aluminum, resulting in a mean X-ray energy of 27.9 keV. An Orca Flash SCMOS detector (Hamamatsu) and a GGG:Eu scintillator with a thickness of 17 μm were used as detectors. Scans were conducted over 360° using 3600 projections with an exposure time of 250 ms. The effective pixel size was 0.9 μm. Reconstructions were performed using custom-made software, namely SYRMEP Tomo Project (STP), as described in previous literature (Brun et al., 2015). To increase the image contrast in the reconstructed images, a phase retrieval algorithm (Paganin et al., 2002) was applied prior to the use of conventional filtered back projection algorithm. The δ/β parameter used for phase retrieval was set at 15.

Additional methods references:

Amado, L.C., Gerber, B.L., Gupta, S.N., Rettmann, D.W., Szarf, G., Schock, R., Nasir, K., Kraitchman, D.L., and Lima, J.A.C., 2004, Accurate and objective infarct sizing by contrast-enhanced magnetic resonance imaging in a canine myocardial infarction model: Journal of the American College of Cardiology, v. 44, p. 2383–2389.

Brun, F., Pacilè, S., Accardo, A., Kourousias, G., Dreossi D., Mancini, L., Tromba, G., Pugliese, R., 2015. Enhanced and Flexible Software Tools for X-ray Computed Tomography at the Italian Synchrotron Radiation Facility Elettra: Fundamenta Informaticae, v. 141, p. 233–243.

Kamber, B., Greig, A., Collerson, K.D., 2006, A new estimate for the composition of weathered young upper continental crust from alluvial sediments, Queensland, Australia: Geochimica et Cosmochimica Acta, v. 69, p. 1041–1058.

Kaufmann, M., 2012. In Poynton, C. (Ed.) The Morgan Kaufmann Series in Computer Graphics: Digital Video and HD (Second Edition), p. 27–36.

Lawrence, M.G., Greig, A., Collerson, K.D., and Kamber, B., 2006, Rare earth element and yttrium variability in South East Queensland waterways: Aquatic Geochemistry, v. 12, p. 39–72.

Paganin, D., Mayo, S.C., Gureyev, T.E., Miller, P.R., and Wilkins, S.W., 2002, Simultaneous phase and amplitude extraction from a single defocused image of a homogeneous object: Journal of Microscopy, v. 206, p. 33–40.

Geological and stratigraphic context
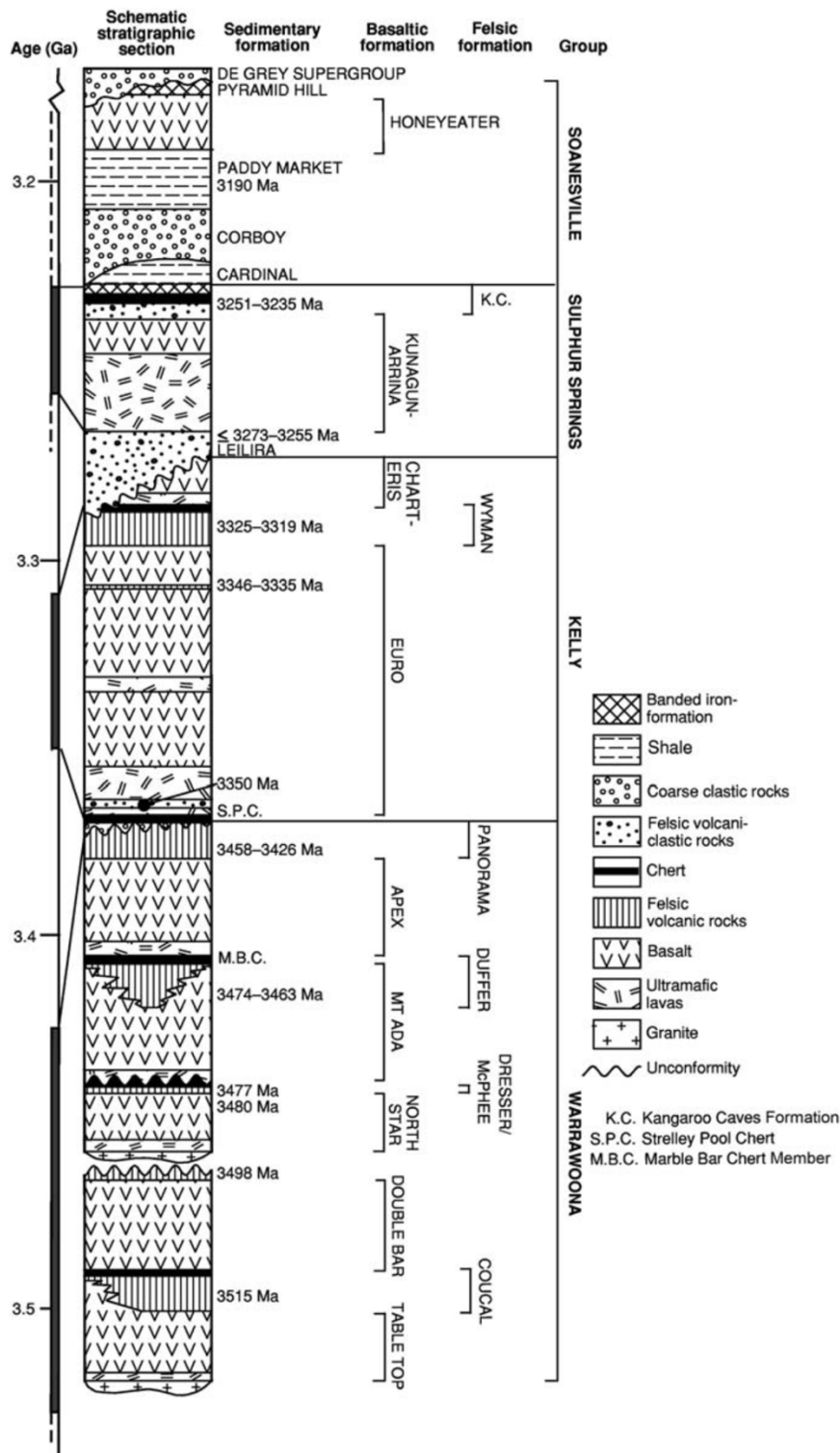
Figure S1. Generalized stratigraphic column of the East Pilbara craton. Age constraints are shown for numerous chert and volcanic horizons; the Dresser Formation (Warrawoona Group) is dated at approximately 3.48 Ga. Adapted from Van Kranendonk et al. (2018).
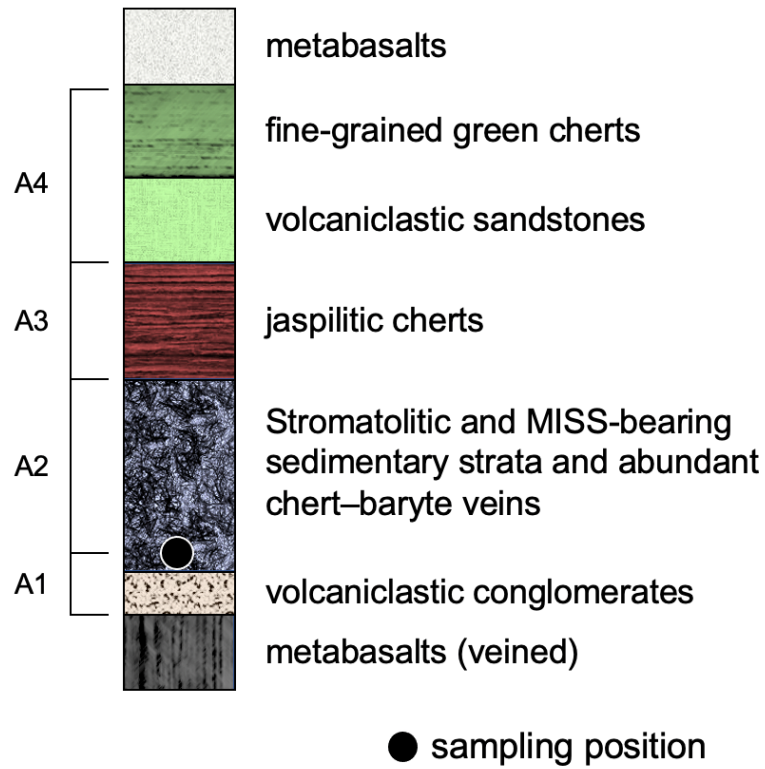
Figure S2. Stratigraphic context of the stromatolite samples studied within the North Pole Chert. Stratigraphic divisions follow the lithostratigraphic assemblages defined by Van Kranendonk et al. (2018) and Djokic et al. (2021).

Optical microscopy
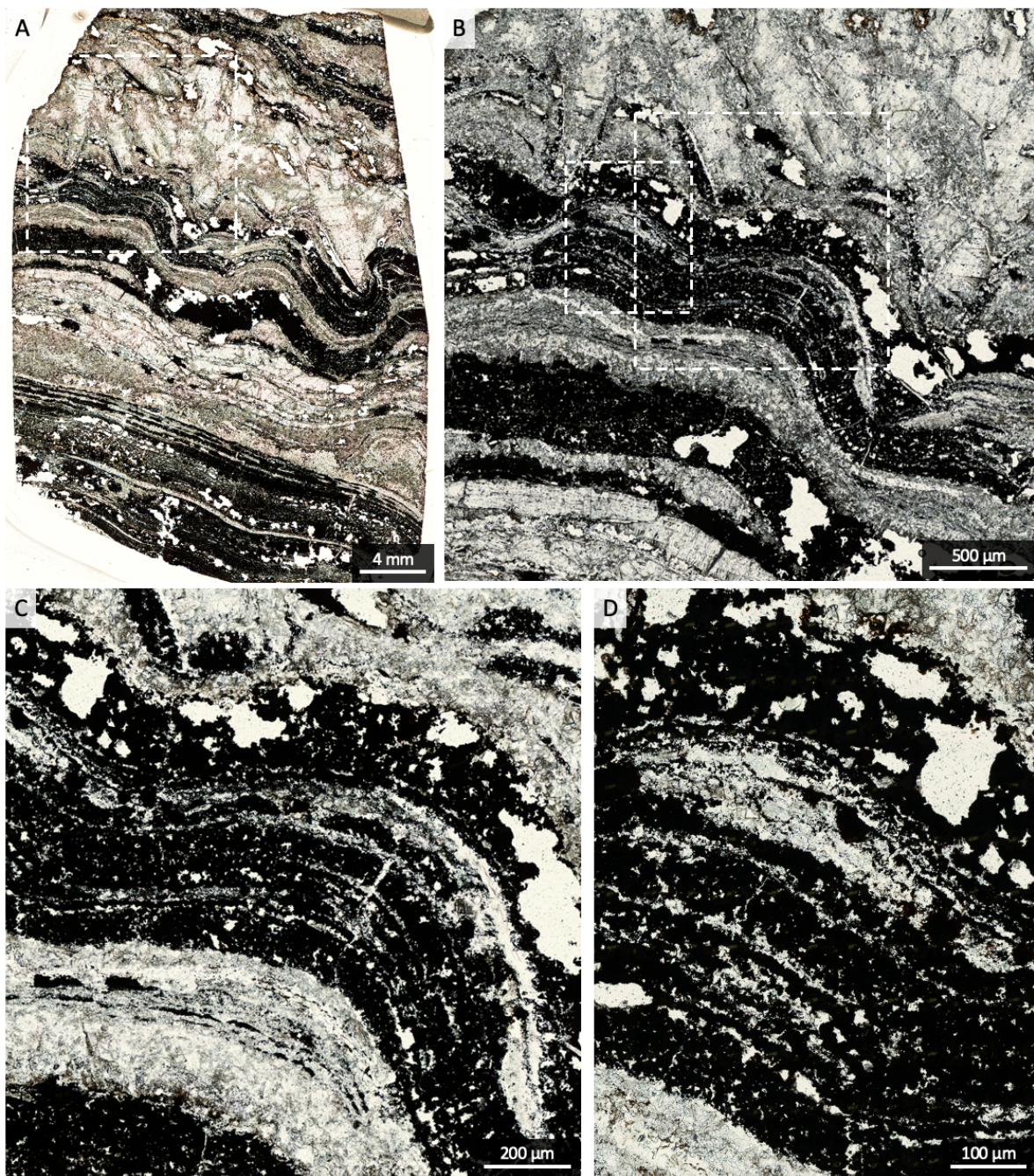
Figure S3. Optical photomicrographs of stratiform–domical Dresser stromatolites. A) Thin section scan. B–C) Higher magnification views of domical stromatolitic fabrics. Undulatory stromatolite layers shown at the right-hand side of A contain palisade structure within a domical stromatolitic fabric; see high-magnification views in Figs. 2C and 3C in the main manuscript.
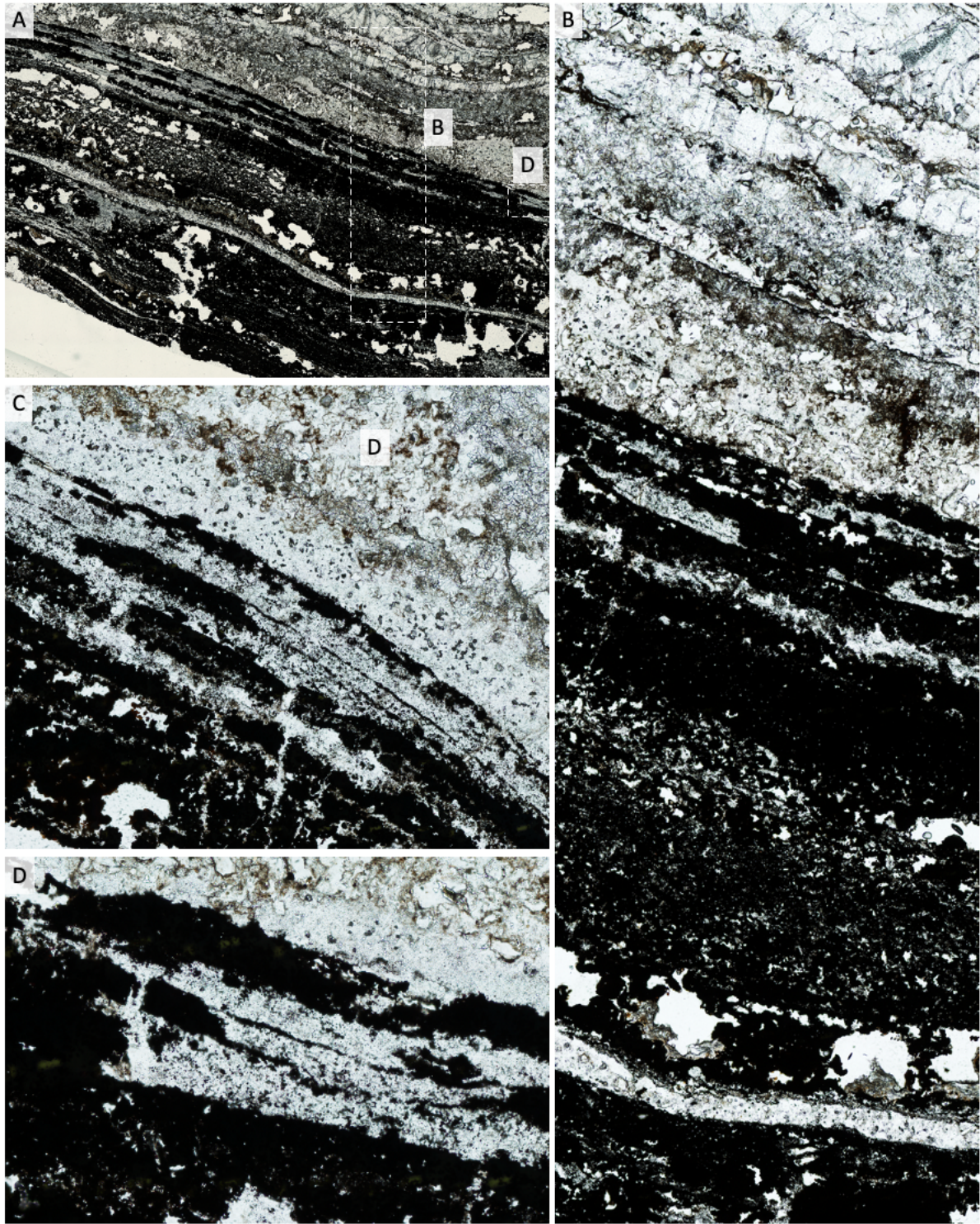
Figure S4. Optical photomicrographs of stratiform Dresser stromatolites. A) Stratiform stromatolite laminations. B) Higher magnification view of a transect through stratiform layers. C–D) Higher magnification views of regions of interest within stratiform stromatolite layers; D corresponds to Fig. 3B in the main manuscript.

LA ICP-MS

Table S1. Concentrations of rare earth elements plus yttrium measured in syndepositional chert bands within Dresser Formation stromatolites.

| No.	La	Ce	Pr	Nd	Sm	Eu	Gd	Tb	Dy	Y	Ho	Er	Tm	Yb	Lu
1	0,059	0,063	0,048	0,033	0,033	0,217	0,057	0,071	0,072	3,108	0,056	0,043	0,066	0,075	0,104
2	0,301	0,200	0,220	0,270	0,548	2,006	0,599	0,806	1,136	0,678	0,975	1,362	0,851	0,729	1,112
3	0,305	0,312	0,241	0,275	0,157	0,643	0,308	0,206	0,109	0,197	0,093	0,164	0,083	0,286	0,406
4	0,523	0,191	0,084	0,154	1,297	27,325	1,009	0,243	0,188	0,440	0,054	0,162	0,259	0,323	0,412
5	0,186	0,231	0,178	0,349	0,461	2,172	1,175	1,313	2,903	4,176	2,664	4,154	4,294	4,215	4,531
6	0,185	0,113	0,098	0,039	0,328	4,892	0,390	0,518	0,345	0,505	0,720	0,558	0,141	0,754	1,531
7	0,852	0,522	0,469	0,222	0,315	2,955	0,363	0,113	0,244	0,272	0,208	0,158	0,282	0,400	0,676
8	0,335	0,118	0,141	0,110	0,337	13,121	0,613	0,095	0,194	0,462	0,185	0,908	0,486	0,489	0,806
9	0,504	0,088	0,089	0,148	0,438	15,860	0,429	0,190	0,147	0,700	0,162	0,132	0,093	0,272	4,061
10	0,164	0,111	0,111	0,042	0,420	13,185	0,730	0,607	0,284	0,587	0,828	0,484	0,812	0,726	2,265

Raman microspectroscopy
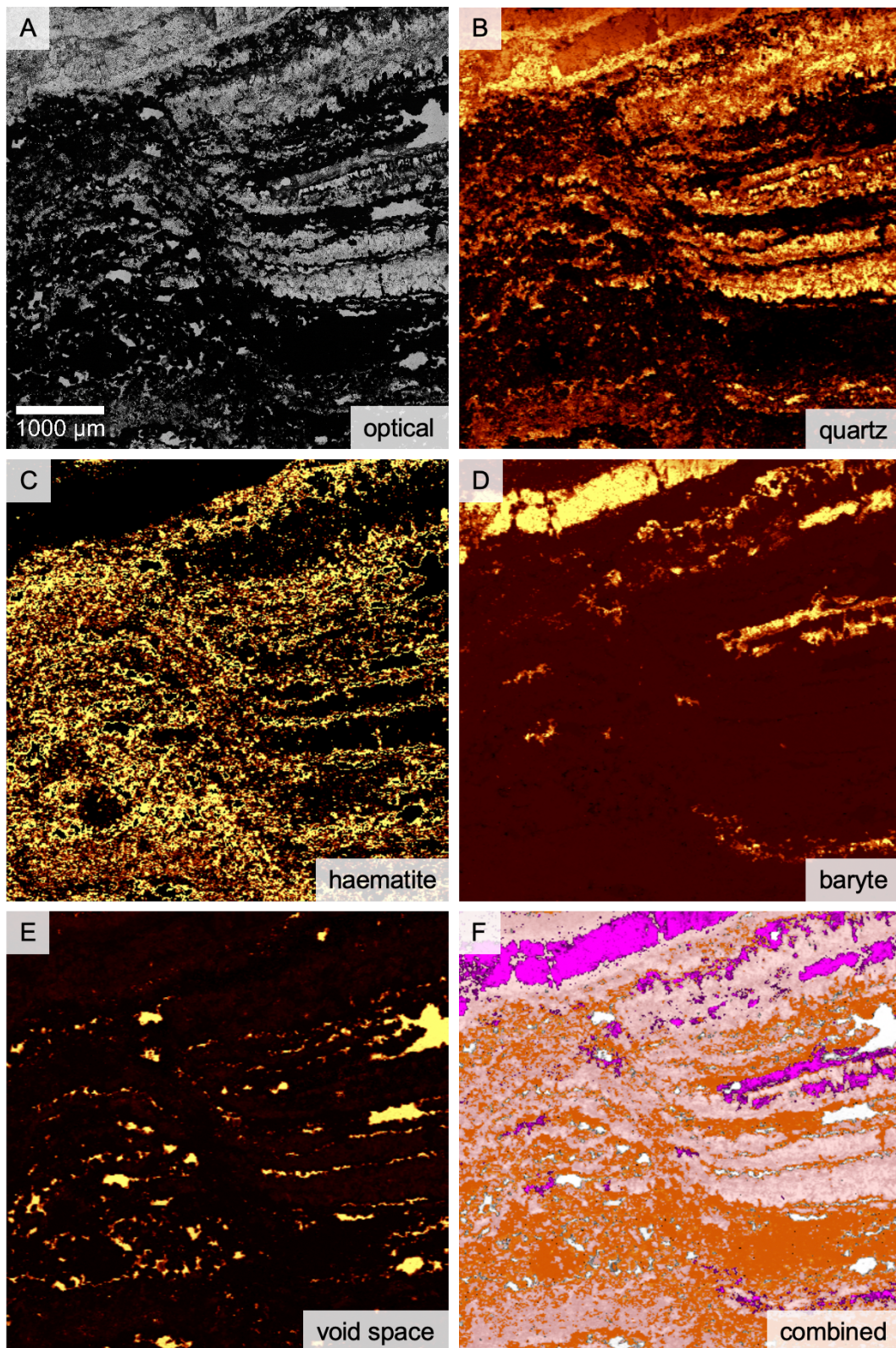
Figure S5. Raman mapping of a domical stromatolite. Images shown correspond to A) optical photomicrograph and B–F) distributions and combination maps of quartz (pink in F), hematite (orange), barite (fuchsia) and void space (white). See Figure 2B in main manuscript.
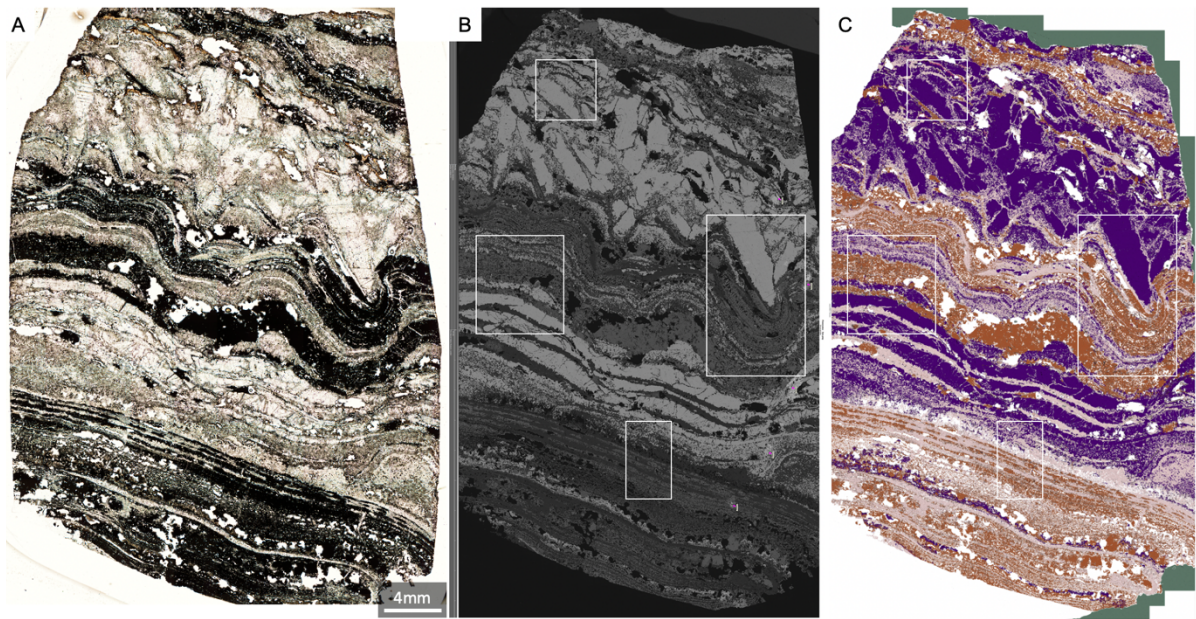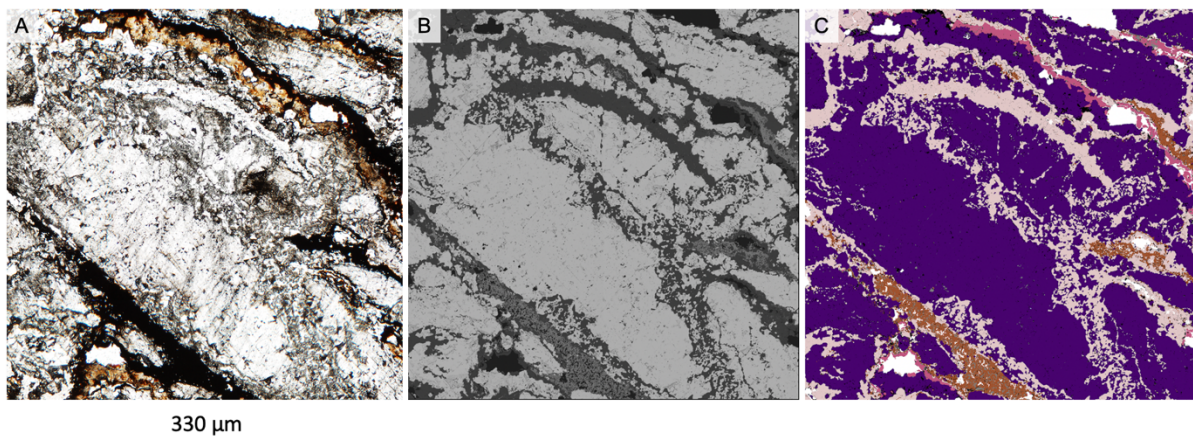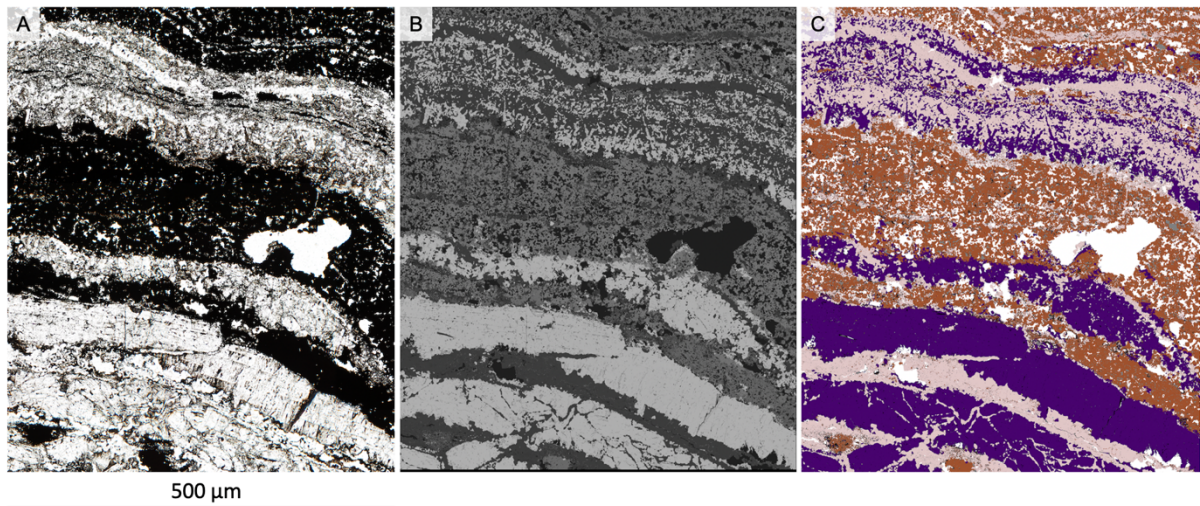
SEM-EDX

Figure S6. Optical image, backscattered electron (BSE) imaging and SEM–EDX mapping of a representative thin section of Dresser Formation stromatolite. Salmon pink = quartz; purple = barite; orange = hematite; white = void space. White boxes show regions of interest analyzed at higher resolution (see Figs. S7–10).

Figure S7. Optical image, backscattered electron (BSE) imaging and SEM–EDX mapping of a representative barite-rich region of Dresser Formation stromatolite. Salmon pink = quartz; purple = barite; orange = hematite; white = void space.

Figure S8. Optical image, backscattered electron (BSE) imaging and SEM–EDX mapping of a representative gently undulatory region of Dresser Formation stromatolite. Note the intimate association between quartz and barite in the upper layers. Salmon pink = quartz; purple = barite; orange = hematite; white = void space.
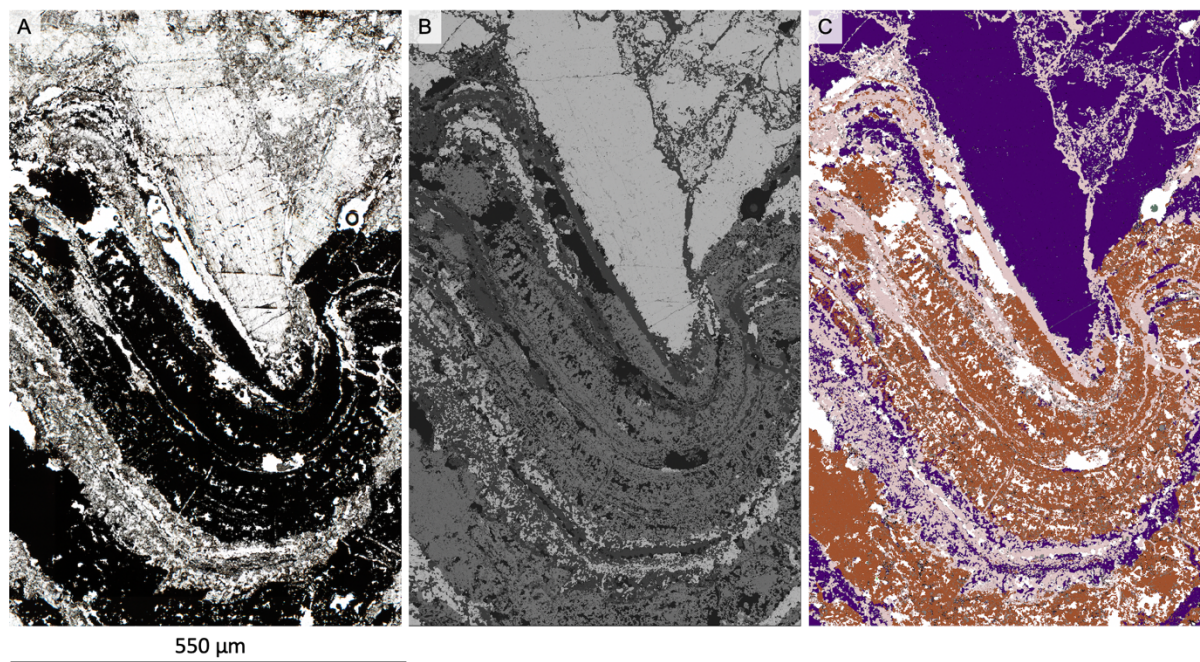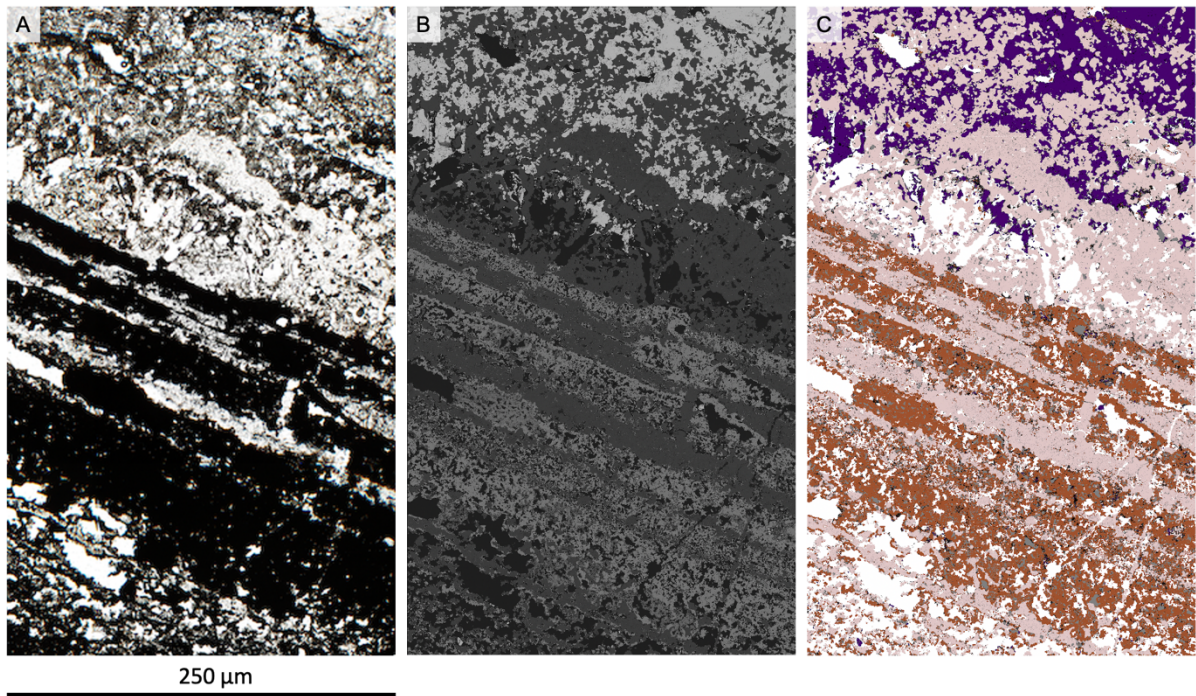

Figure S9. Optical image, backscattered electron (BSE) imaging and SEM–EDX mapping of a representative undulatory region of Dresser Formation stromatolite. Salmon pink = quartz; purple = barite; orange = hematite; white = void space.
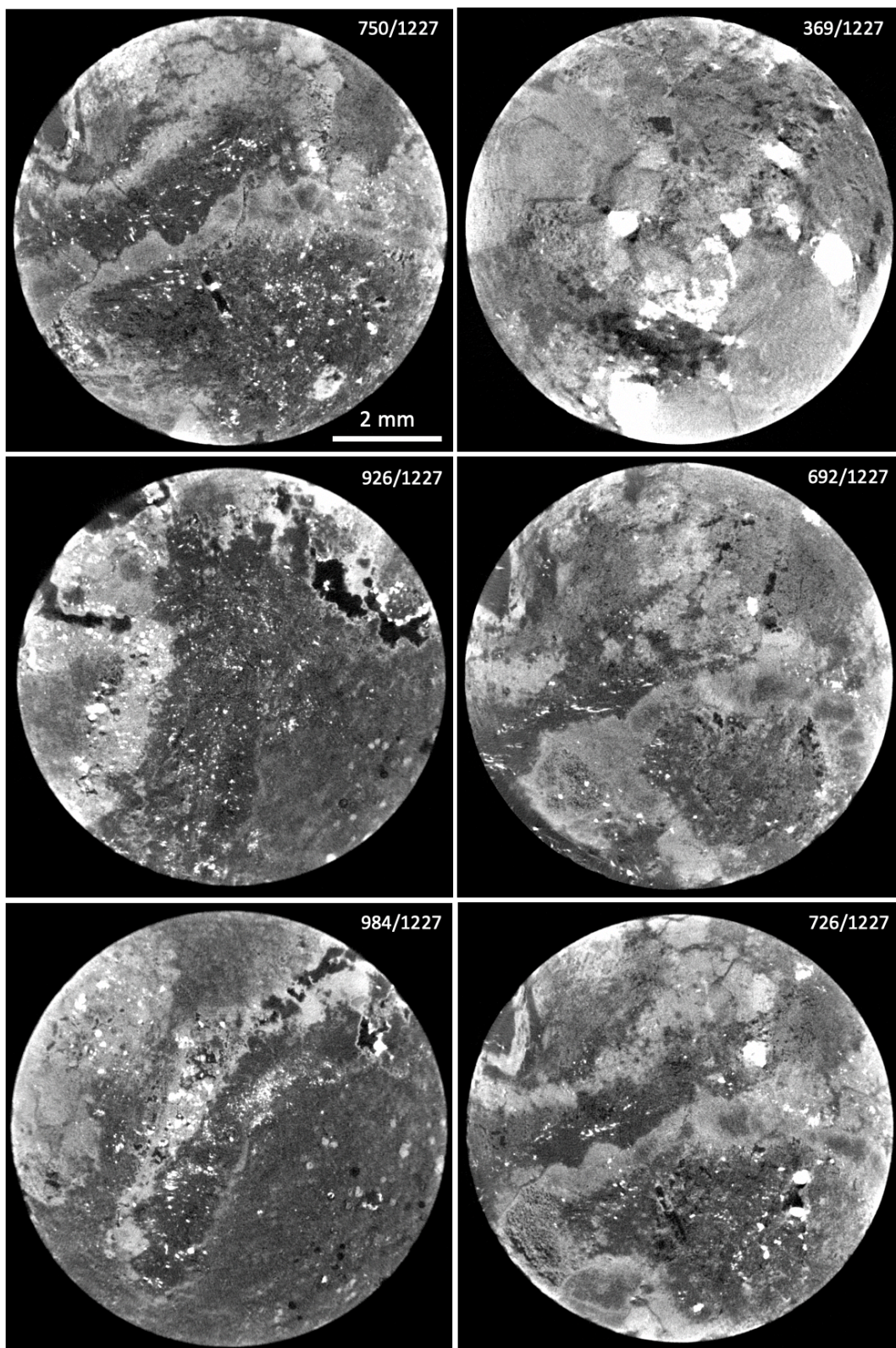
Figure S10. Optical image, backscattered electron (BSE) imaging and SEM–EDX mapping of a representative stratiform region of Dresser Formation stromatolite. Salmon pink = quartz; purple = barite; orange = hematite; white = void space.

Figure S11. Representative SEM-EDX spectra of hematite (A), quartz (B) and barite (C). Peak identifications are shown.

Laboratory X-ray μCT

Figure S12. Representative laboratory X-ray μCT tomograms (voxel resolution = 6.5 μm) within a Dresser Formation stromatolite sample. Lighter colours correspond to higher densities.
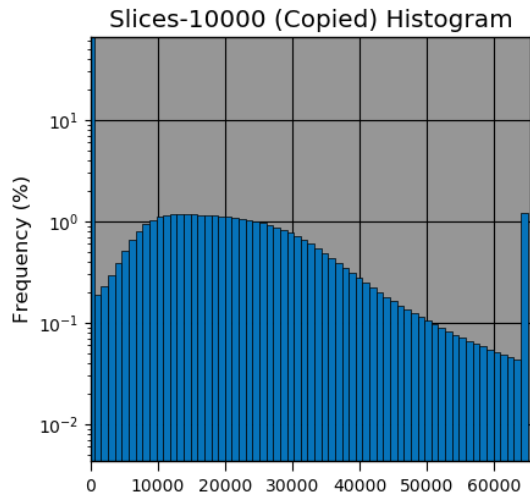
Figure S13. Histogram corresponding to the entire volume of the Dresser Formation sample studied using laboratory X-ray μCT.
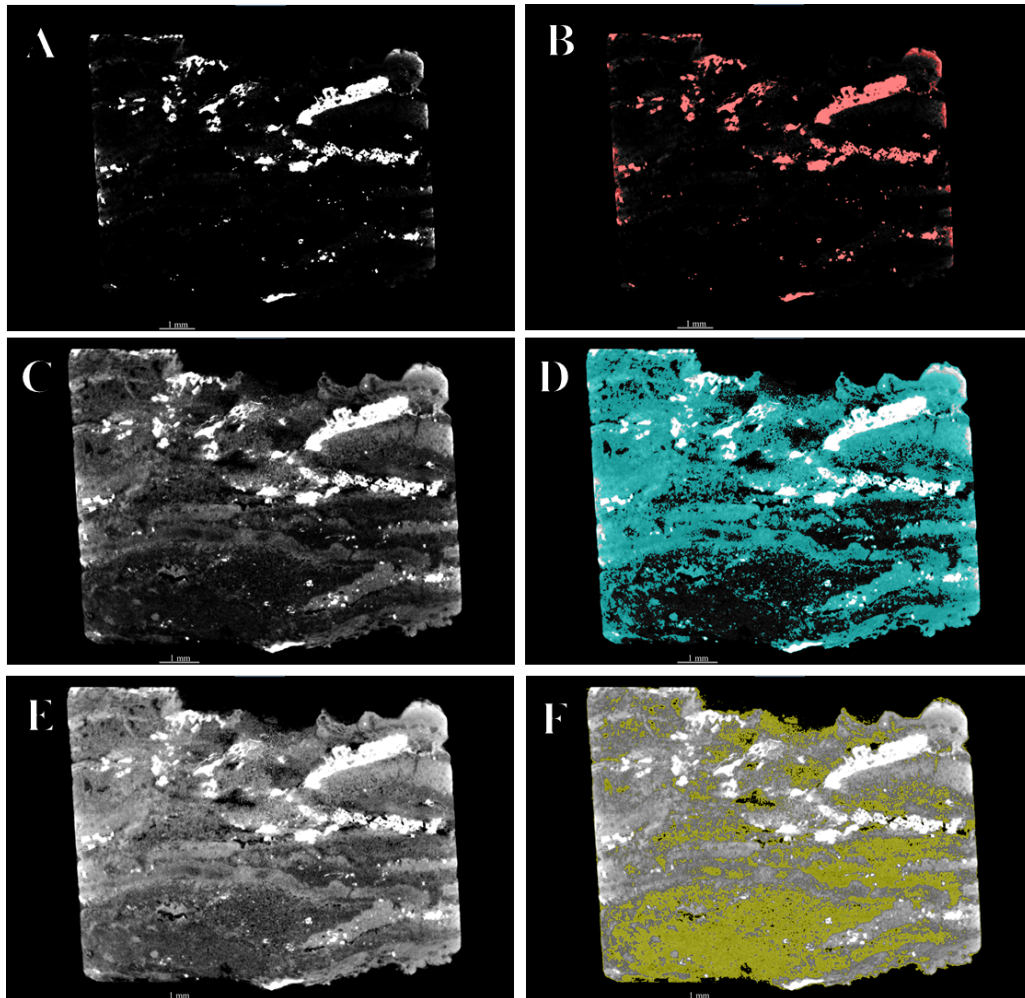

Figure S14. YZ slices of the Dresser Formation sample studied using laboratory X-ray μCT and phases segmentation; grey level images (A, C, E) are adjusted using gamma ratios of 0.2, 0.7 and 1.4, respectively. B) hematite. D) barite. F) quartz. Sample is 8 mm in diameter.
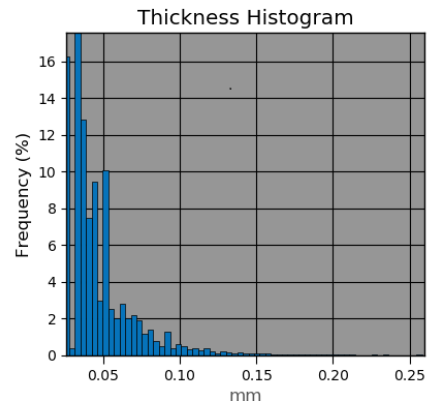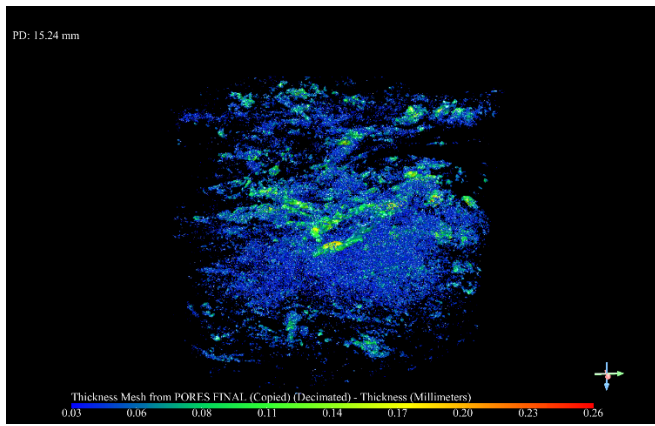
Figure S15. Segmented pores (void spaces) of Dresser Formation stromatolite and pore size distribution. Sample is 8 mm in diameter.
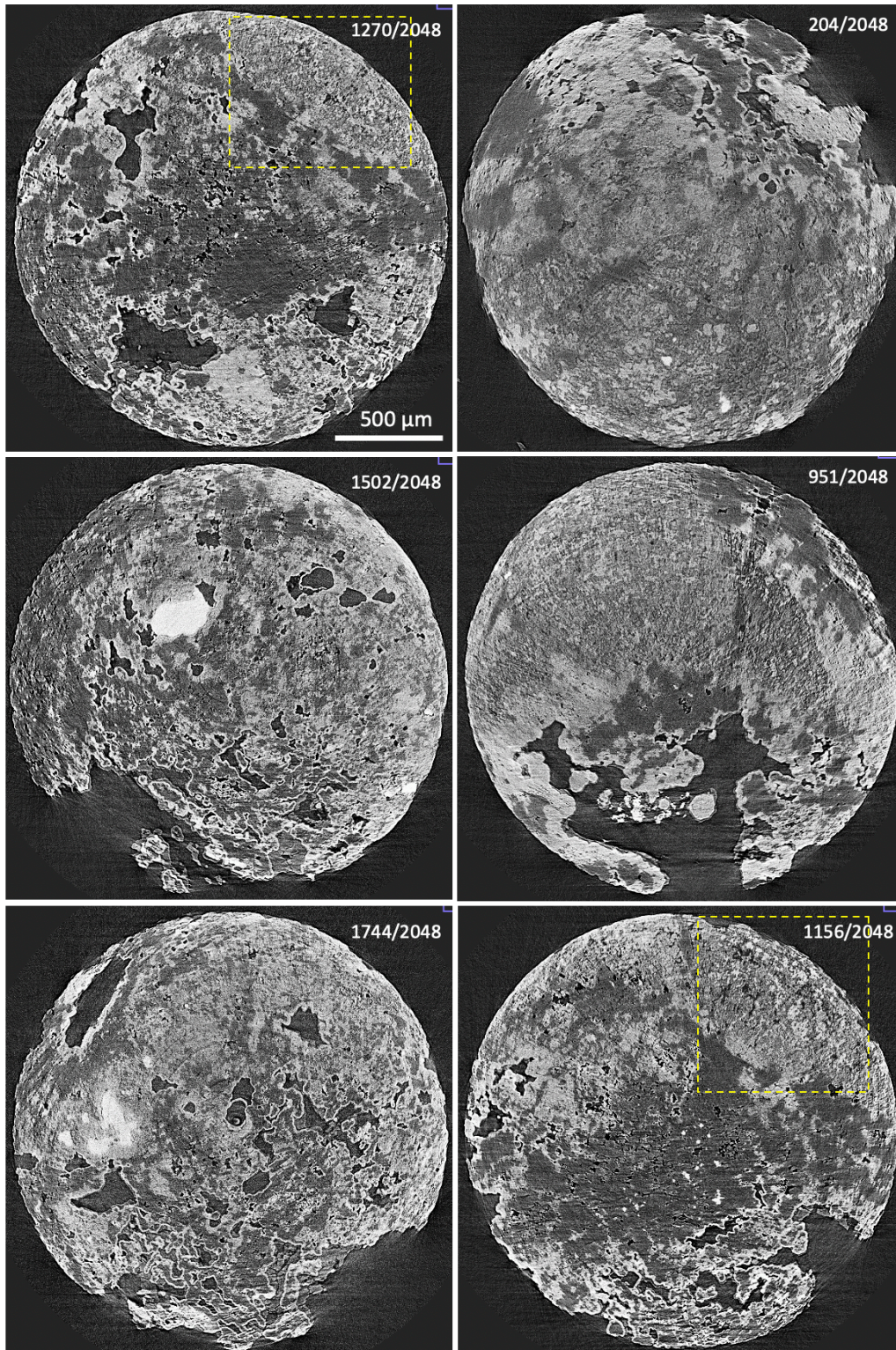
Synchrotron X-ray µCT

Figure S16. Representative synchrotron X-ray µCT tomograms (voxel resolution = 0.9 µm) within a Dresser Formation stromatolite sample. Lighter colors correspond to higher densities. Note the highest-density hematite veneer at the external margins of the sample. Yellow boxes highlight zones corresponding to palisade structure in 3D renderings.